

Enhanced electronic and photoelectrical properties of two-dimensional Zn-doped SnS_2

Xichen Chuai(揣喜臣), Peng Yin(殷鹏), Jiawei Wang(王嘉玮), Guanhua Yang(杨冠华), Congyan Lu(陆丛研), Di Geng(耿玓), Ling Li(李泠), Can Liu(刘灿), Zhongming Wei(魏钟鸣), and Nianduan Lu(卢年端)

Citation : Chin. Phys. B, 2025, 34 (**5**): 056101. DOI: 10.1088/1674-1056/adbaca
http://cpb.iphy.ac.cn; http://iopscience.iop.org/cpb

What follows is a list of articles you may be interested in

Microstructure and magnetic properties of FeCoZr(Mo)BGe nanocrystalline alloys

Wanqiu Yu(于万秋), Yanxiang Sun(孙筵翔), Lihua Liu(刘立华), and Pingli Zhang(张平丽)
Chin. Phys. B, 2025, 34 (**1**): 016102. DOI: 10.1088/1674-1056/ad5a77

Enhanced mechanical and thermal properties of two-dimensional SiC and GeC with temperature and size dependence

Lei Huang(黄磊), Kai Ren(任凯), Huanping Zhang(张焕萍), and Huasong Qin(覃华松)
Chin. Phys. B, 2023, 32 (**7**): 076103. DOI: 10.1088/1674-1056/acc78f

Boosting the performance of crossed ZnO microwire UV photodetector by mechanical contact homo-interface barrier

Yinzhe Liu(刘寅哲), Kewei Liu(刘可为), Jialin Yang(杨佳霖), Zhen Cheng(程祯), Dongyang Han(韩冬阳), Qiu Ai(艾秋), Xing Chen(陈星), Yongxue Zhu(朱勇学), Binghui Li(李炳辉), Lei Liu(刘雷), and Dezhen Shen(申德振)
Chin. Phys. B, 2022, 31 (**10**): 106101. DOI: 10.1088/1674-1056/ac80b0

Suppression of persistent photoconductivity in high gain Ga_2O_3 Schottky photodetectors

Haitao Zhou(周海涛), Lujia Cong(丛璐佳), Jiangang Ma(马剑钢), Bingsheng Li(李炳生), Haiyang Xu(徐海洋), and Yichun Liu(刘益春)
Chin. Phys. B, 2021, 30 (**12**): 126104. DOI: 10.1088/1674-1056/ac2d1b

Review of improved spectral response of ultraviolet photodetectors by surface plasmon

You Wu(吴忧), Xiao-Juan Sun(孙晓娟), Yu-Ping Jia(贾玉萍), Da-Bing Li(黎大兵)
Chin. Phys. B, 2018, 27 (**12**): 126101. DOI: 10.1088/1674-1056/27/12/126101

Enhanced electronic and photoelectrical properties of two-dimensional Zn-doped SnS_2

Xichen Chuai(揣喜臣)[1,2], Peng Yin(殷鹏)[3,4], Jiawei Wang(王嘉玮)[1], Guanhua Yang(杨冠华)[1], Congyan Lu(陆丛研)[1], Di Geng(耿玓)[1], Ling Li(李泠)[1], Can Liu(刘灿)[4,†], Zhongming Wei(魏钟鸣)[3,‡], and Nianduan Lu(卢年端)[1,§]

[1] *Laboratory of Microelectronics Device & Integrated Technology, Institute of Microelectronics, Chinese Academy of Sciences, Beijing* 100029, *China*
[2] *University of Chinese Academy of Sciences, Beijing* 100049, *China*
[3] *State Key Laboratory of Superlattices and Microstructures, Institute of Semiconductors, Chinese Academy of Sciences, Beijing* 100083, *China*
[4] *School of Physics, Renmin University of China, Beijing* 100872, *China*

(Received 30 November 2024; revised manuscript received 12 January 2025; accepted manuscript online 27 February 2025)

Alloy engineering, with its ability to tune the electronic band structure, is regarded as an effective method for adjusting the electronic and optoelectronic properties of two-dimensional (2D) semiconductors. However, synthesizing metal-site substitution alloys remains challenging due to the low reactivity of metal precursors and the tendency for spatial phase separation during high-temperature growth. Here, we report the preparation of a high-quality metal-site substitution alloy, $Zn_{0.167}Sn_{0.833}S_2$, via the chemical vapor transport method, which exhibits excellent photoresponsivity and enhanced electrical transport properties. Comprehensive characterization techniques, including Raman spectroscopy, x-ray photoelectron spectroscopy (XPS), and electron microscopy, unambiguously confirm the uniform Zn substitution in the as-prepared $Zn_{0.167}Sn_{0.833}S_2$ alloy. Furthermore, the photodetector based on the $Zn_{0.167}Sn_{0.833}S_2$ alloy demonstrated a high on/off ratio of 51 under white light, a wide spectral response range from 350 nm to 900 nm, and a broad dynamic power range of 80 dB under 638-nm illumination. In terms of transport properties, field-effect transistors (FETs) based on $Zn_{0.167}Sn_{0.833}S_2$ achieved a carrier mobility of 6.5 $cm^2 \cdot V^{-1} \cdot s^{-1}$, which is six times higher than that of SnS_2. This alloy semiconductor showcases significantly enhanced electronic and optoelectronic properties, offering great potential for the development of high-resolution photodetection technologies.

Keywords: alloy engineering, metal-site substitution, photodetector, field-effect transistors

PACS: 61.43.Dq, 74.62.Dh, 85.60.Gz, 85.30.Tv

DOI: 10.1088/1674-1056/adbaca **CSTR:** 32038.14.CPB.adbaca

1. Introduction

Two-dimensional (2D) materials, including graphene, hexagonal boron nitride (hBN), transition-metal dichalcogenides, and group III–V semiconductors, have garnered significant attention over the past two decades due to their unique electronic band structures, particularly spin-valley coupling, and exceptional charge transfer properties, making them promising candidates for next-generation electronic and optoelectronic devices.[1–8] Various synthesis methods for 2D layered materials have emerged to prepare monolayer, few-layer and bulk materials,[9] including molecular beam epitaxy (MBE),[10] chemical vapor deposition (CVD),[11,12] metal–organic chemical vapour deposition (MOCVD), physical vapor deposition (PVD), and chemical vapor transport (CVT).[13] Among these, the CVT method is particularly well-suited for the growth of high-quality bulk crystals, owing to its ability to promote crystal growth relaxation over several tens of days. To date, hundreds of 2D layered crystals have been discovered, exhibiting a broad range of physical properties, spanning from semimetals and semiconductors to insulators.

The tunable electronic band structures of 2D materials offer significant flexibility in modifying various physical properties, including carrier mobility, band gap characteristics, and photon transition behaviors. These properties can be effectively tailored through defect engineering,[14] heterostructure engineering,[15–17] and component engineering.[18,19] In component engineering, the incorporation of specific components enables precise bandgap tuning, which is essential for applications in photonics, optoelectronics, and light emission. Specifically, alloying at metal sites can influence the deep-level distribution of the valence band, thereby promoting photogenerated carrier transitions and enhancing the performance of sensors and photodetectors. For instance, $Mo_{1-x}W_xS_2$ exhibits large photocurrents that are four times higher than those of WS_2 and MoS_2.[20] Additionally, $Mo_{1-x}W_xSe_2$ demonstrates layer-number-dependent band energies and broad-spectrum detection capabilities.[21] Furthermore, the 2D ternary compound $Ga_2In_4S_9$ exhibits excellent ultraviolet (UV) detection

†Corresponding author. E-mail: lunianduan@ime.ac.cn
‡Corresponding author. E-mail: zmwei@semi.ac.cn
§Corresponding author. E-mail: canliu@ruc.edu.cn

© 2025 Chinese Physical Society and IOP Publishing Ltd. All rights, including for text and data mining, AI training, and similar technologies, are reserved.

ability with rapid response times.[22]

In this study, we propose the fabrication of $Sn_{1-x}Zn_xS_2$ alloys to tune the bandgap of SnS_2 crystals, thereby achieving high-performance photodetectors with enhanced responsivity, a large linear response, and a broad spectral range. The 2D layered SnS_2 crystal is a member of the II–VI group semiconductors and exhibits unique carrier mobility of 0.1 $cm^2 \cdot V^{-1} \cdot S^{-1}$–40 $cm^2 \cdot V^{-1} \cdot S^{-1}$ and a photoresponsivity of $\sim 10^5$ $mA \cdot W^{-1}$.[23–25] However, the intrinsic wide bandgap structure of SnS_2 limits its potential in optical applications.[26,27] To overcome this, we use Zn as an active metal for site substitution, which allows for the adjustment of the band alignment in SnS_2. Using chemical vapor transport (CVT), we successfully synthesized high-quality $Z_xSn_{1-x}S_2$ ($x = 0.167$) alloy bulk materials. Notably, both the carrier mobility and the photoresponse ability are significantly enhanced in the alloyed crystals.

2. Method

2.1. Chemical vapor transport for alloy prepared

The elements sulfur (S), tin (Sn), and zinc (Zn) were used as reaction precursors and thoroughly mixed in a vacuum-evacuated glass ampoule with a molar mass ratio of 10:30:0.6. Additionally, 2 moles of elemental iodine (I) were added as a catalyst. The mixture was sealed in a glass ampoule with 18 mm in diameter and 20 cm in length under vacuum conditions. The ampoule was placed in a two-zone furnace, with the reactants positioned in the high-temperature zone ($T =$ 650 °C) to facilitate crystal growth in the low-temperature zone ($T = 600$ °C) over three days. Afterward, the furnace temperature was gradually reduced at a rate of 10 °C per hour while maintaining a 50-°C difference between the two zones. This controlled process successfully produced high-quality $Zn_{0.167}Sn_{0.833}S_2$ alloy crystals.

2.2. Back-gating field-effect transistors

To fabricate $Zn_{0.167}Sn_{0.833}S_2$ field-effect transistors (FETs), few-layer $Zn_{0.167}Sn_{0.833}S_2$ was mechanically exfoliated onto an SiO_2/Si substrate using adhesive tape. The substrate comprised a highly doped n-type silicon wafer with 300 nm in thick SiO_2 capping layer. A gold stripe mask was transferred onto the $Zn_{0.167}Sn_{0.833}S_2$ few layers before deposition gold electrodes. After lift off the gold stripe mask, the channel was obtained. Following the lift-off of the gold stripe mask, the channel region was formed. Next, the electrodes of source and drain were separated by the probe station.

3. Results and discussion

3.1. Synthesis of $Zn_{0.167}Sn_{0.833}S_2$ semiconductor alloy crystal

High-quality $Zn_xSn_{1-x}S_2$ alloy bulk crystals were synthesized using the CVT method. A schematic diagram of the synthesis process is shown in Fig. 1(a). The crystal structure of the $Zn_xSn_{1-x}S_2$ alloys, as shown in Fig. 1(b), belongs to triclinic crystal system with $P\bar{3}m1$ space group.

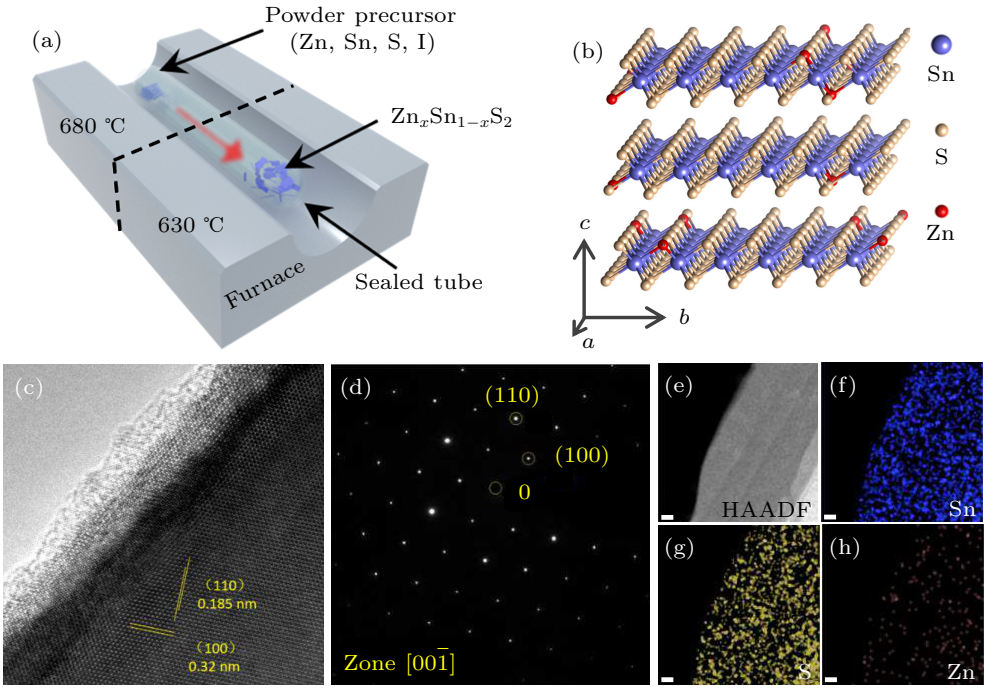


Fig. 1. Growth of $Zn_{0.167}Sn_{0.833}S_2$ alloy materials via the CVT method. (a) Schematic diagram of the experimental setup for synthesizing bulk alloy crystals through the CVT process, (b) crystal structures of $Zn_{0.167}Sn_{0.833}S_2$ alloys, (c)–(d) atomically resolved transmission electron microscopy (TEM) image (c) and selected area electron diffraction (SAED) pattern (d) of high-quality $Zn_{0.167}Sn_{0.833}S_2$ film, oriented along the [00$\bar{1}$] crystal axis, (e)–(h) high-angle annular dark-field (HAADF) image (e) and energy-dispersive x-ray spectroscopy (EDS) elemental mapping of Sn (f), S (g), and Zn (h), confirming the uniform distribution of Zn within the alloy.

To characterize the microstructure and crystallinity of $Zn_xSn_{1-x}S_2$ alloy crystals, transmission electron microscopy (TEM) and were employed. High resolution TEM (HRTEM) image (Fig. 1(c)) reveals that the $Zn_xSn_{1-x}S_2$ alloy crystal remains the lattice configuration of SnS_2, with lattice spacings of 0.184 nm and 0.32 nm corresponding to the (110) and (100) planes, demonstrating the Zn metal sits substitution in alloy material. The selected area electron diffraction (SAED) pattern (Fig. 1(d)) distinctly displays a hexagonally arranged spot pattern, indicative of the triclinic crystal system oriented along the [00–1] zone axis, underscoring the high crystallization quality of the alloy. Furthermore, the high-angle annular dark-field (HAADF-STEM) image (Fig. 1(e)), with a 100-nm scale bar, confirms the absence of clusters in the alloy crystal, further supporting its structural homogeneity. Energy-dispersive x-ray spectroscopy (EDS) elemental mapping of S, Sn, and Zn (Figs. 1(f)–1(h)) confirms the uniform distribution of Zn throughout the alloy crystal, as evident in the EDS mapping of Zn (Fig. 1(h)). These findings collectively demonstrate the well-ordered microstructure and compositional homogeneity of the $Zn_xSn_{1-x}S_2$ alloy.

3.2. Identification of elemental composition in $Zn_xSn_{1-x}S_2$ alloys

Raman spectroscopy is a widely employed technique for confirming the crystal structure of 2D materials by analyzing lattice vibration peaks.[28–31] The thickness-dependent Raman spectral of $Zn_{0.167}Sn_{0.833}S_2$ nanosheets were measured and shown in Fig. 2(b). Two prominent Raman peaks are observed in the range of 200 cm^{-1}–400 cm^{-1} under a 532-nm excitation wavelength, corresponding to SnS_2 at 313 cm^{-1} and Zn^{2+} at 353 cm^{-1}. The peak at 313 cm^{-1} is attributed to the A_{1g} vibrational mode of SnS_2, while the peak at 353 cm^{-1} is assigned to the E_1 mode of Zn^{2+},[32] confirming the Zn–S bonds within the crystal structure.

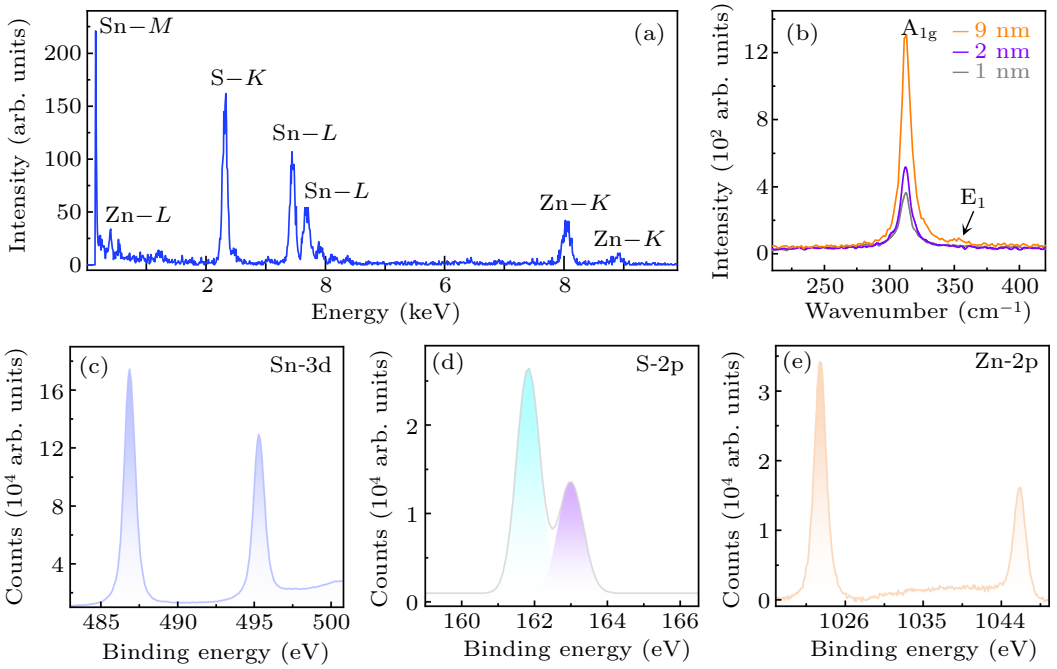


Fig. 2. Identification of elemental composition in $Zn_{0.167}Sn_{0.833}S_2$ alloys: (a) energy-dispersive x-ray spectroscopy (EDS) analysis of $Zn_{0.167}Sn_{0.833}S_2$ alloys flake on a copper grid substrate, (b) thickness-dependent Raman spectra of $Zn_{0.167}Sn_{0.833}S_2$ nanosheets, (c)–(e) x-ray photoelectron spectroscopy (XPS) analysis of the alloy, including the Sn 3d (c), S 2p (d), and Zn 2p (e) regions. The elemental composition of $Zn_{0.167}Sn_{0.833}S_2$ is confirmed by the peak area ratios in these spectra.

3.3. The optoelectronic properties of $Zn_{0.167}Sn_{0.833}S_2$ alloy

To investigate the photoresponse of $Zn_{0.167}Sn_{0.833}S_2$ alloy, a two-terminal photodetector (Fig. 3(a)) was fabricated and then excited by the white LED and different wavelength lasers. As shown in Fig. 3(b), the photodetector exhibited a high on/off ratio of 51 under white light illumination, indicating that the alloy is the excellent light-sensitive material. Additionally, wavelength-dependent photocurrents were measured under the same power density of 250 $\mu W/cm^2$, demonstrating significant responsiveness in the visible light and cut-off response at 860 nm. From the scatter diagram in Fig. 3(c), the optimal response wavelength is located in 740 nm, corresponding to the responsivity (R) of 2.3×10^5 $mA\cdot W^{-1}$ and an external quantum efficiency (EQE) as high as $3.6\times10^5\%$. Indeed, the R and EQE were calculated using the following formulas: $R = I_{ph}/(p \times s)$ and $EQE = hcR/(e\lambda)$, where I_{ph} is the photocurrent, P is the power density of the incident light, S is the effective illuminated area, h is the Planck's constant, c is the speed of light, λ is the wavelength of excitation light, and e is the elementary electronic charge. Additionally, the photodetector performance of reported SnS_2 is summarized in Table 1, which compares it with the $Zn_{0.167}Sn_{0.833}S_2$ alloy-based pho-

todetector. The comparison highlights that the Zn-doped SnS_2 alloy exhibits a broadened response wavelength range extending into the near-infrared wavelength (860 nm) and enhanced photoresponse characteristics.

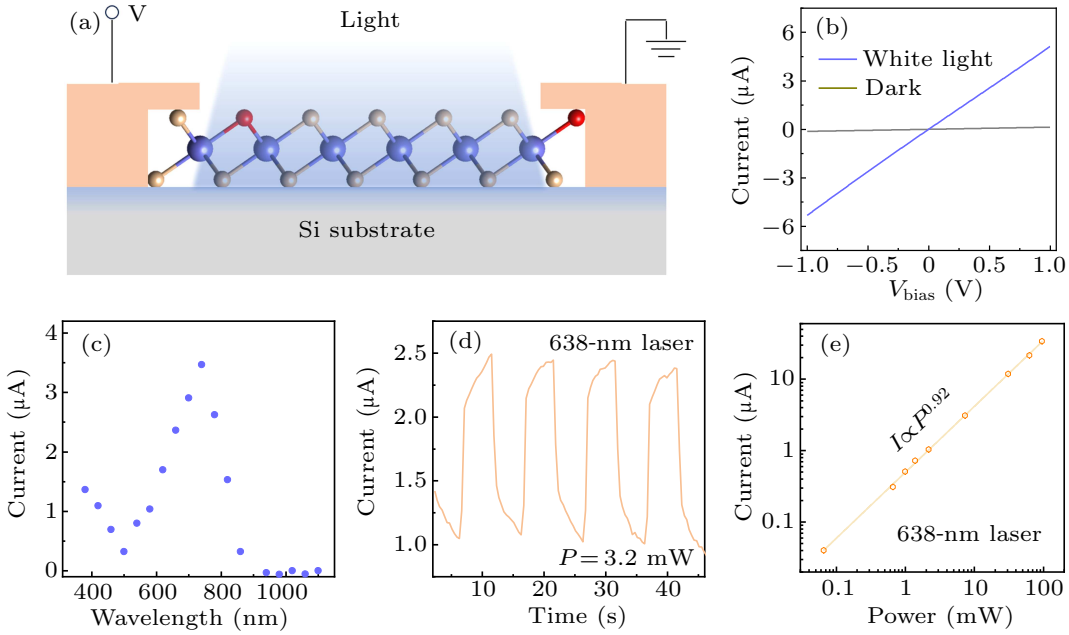


Fig. 3. Photoelectronic characterization of $Zn_{0.167}Sn_{0.833}S_2$ alloy: (a) the side view schematic of $Zn_{0.167}Sn_{0.833}S_2$-based photodetector, (b) representative *I*–*V* characteristics measured under the white LED illumination, (c) wavelength-dependent photocurrents with the step of 40 nm, (d) time-resolved stability under 638-nm laser illumination, (e) incident-power-dependence photocurrents at 638-nm laser illumination.

Table 1. Photodetector performance of alloy in this work compared with reported SnS_2.

Photodetector	Response wavelength (nm)	Responsivity (mA·W^{-1})	External quantum efficiency (%)	LDR (dB)	References
FL SnS_2	532	100	–	–	[23]
FL SnS_2	300–550	2.6×10^5	9.3×10^4	20	[33]
100 nm-SnS_2	405	3.54×10^5	1.1×10^5	< 10	[25]
FL SnS_2	380-660	184	513	< 10	[34]
FL $Zn_{0.167}Sn_{0.833}S_2$	380–860	2.3×10^5	3.6×10^5	80	this work

Indeed, the laser of 638 nm was utilized to excite photocurrents, exhibiting a stable and time-resolved switching response, as shown in Fig. 3(d). Moreover, power-dependent photocurrent measurements revealed an exceptional linear dynamic range (LDR) of 80 dB (Fig. 3(e)), which is much higher than that of SnS_2, underscoring the superior performance of the $Zn_{0.167}Sn_{0.833}S_2$ alloy-based photodetector.

3.4. Electronic transport properties of $Zn_{0.167}Sn_{0.833}S_2$ FETs

To study the electrical properties of alloy materials, back-gating FET device was fabricated (Fig. 4(a), see Section 2). The size of $Zn_{0.167}Sn_{0.833}S_2$ FET was determined using the atomic force microscopy (AFM) image (Fig. 4 (b)). The length and width of the FET channel are 2.6 μm and 5 μm respectively, and the thickness of $Zn_{0.167}Sn_{0.833}S_2$ nanoflake is 11 nm.

The transfer curve is shown in Fig. 4(c) sweeping the V_{gs} value from −50 V to 50 V with the V_{ds} value of 0.1 V. In the transfer curve, the left *y*-axis uses linear coordinate system, while the right *y*-axis is displayed on a $\log_{10}$ scale. The $Zn_{0.167}Sn_{0.833}S_2$-based FET shows typical n-type behavior and belongs to depletion transistor. The field-effect mobility (μ_m) could be calculated by the formula

$$\mu_m = \frac{\partial I_{ds}}{\partial V_g} \cdot \frac{L}{W C_g V_{ds}},$$

where I_{ds} is the current between source and drain, V_{ds} is the voltage from drain side to source side, V_g is the gate voltage added on the high doping silicon substrate, L is the length of channel, W is the width of channel, C_g ($C(SiO_2) = 11.6$ nF cm^{-2}) is gate capacitance parameter of 300-nm SiO_2 layer. By analyzing the data in Figs. 4(c) and 4(d), the electron mobility of $Zn_{0.167}Sn_{0.833}S_2$ FET is calculated to be 6.5 cm^{2}V^{-1}·s^{-1}, which is six times higher than that of SnS_2 (1.1 cm^2·V^{-1}·s^{-1}), as the same channel thickness (∼ 11 nm). Meanwhile, the saturation current of $Zn_{0.167}Sn_{0.833}S_2$ alloy is an order of magnitude higher than that of SnS_2. Further, the output curves of $Zn_{0.167}Sn_{0.833}S_2$ FET, shown in Fig. 4(e), exhibit a linear relationship, indicating Ohmic contact between the gold electrodes and the $Zn_{0.167}Sn_{0.833}S_2$ nanoflakes.

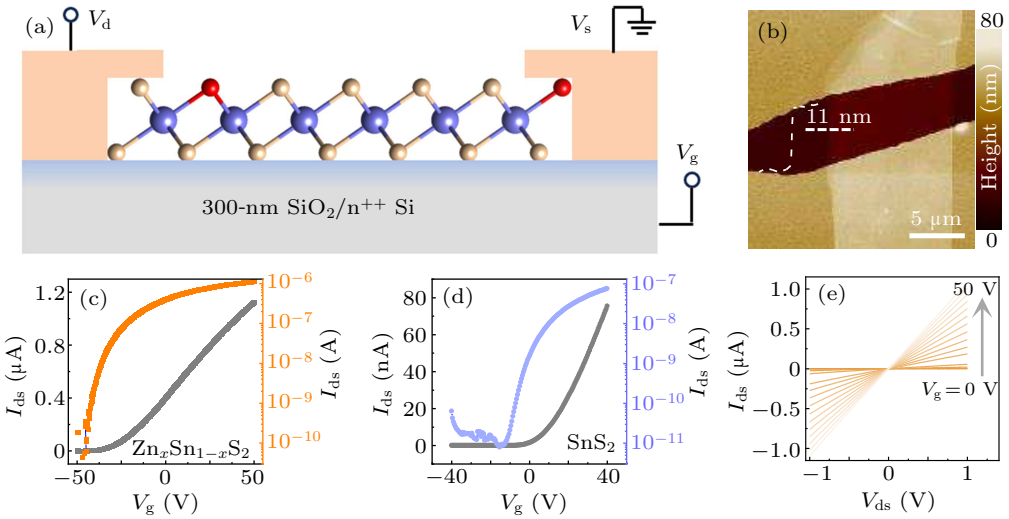


Fig. 4. Electronic characterization of $Zn_{0.167}Sn_{0.833}S_2$ alloy: (a) the side view schematic of $Zn_{0.167}Sn_{0.833}S_2$-based FETs, (b) experimental AFM image of $Zn_{0.167}Sn_{0.833}S_2$ FET device with the nanosheets thickness of 11 nm, (c)–(d) transfer characteristics of the back-gate-regulated $Zn_{0.167}Sn_{0.833}S_2$ FET (c) and SnS_2 FET (d), (e) the output curves from the gating bias 0 V to 50 V under the source-drain bias voltage of 0.1 V.

3.5. Theory section

The first principles calculation based on density functional theory (DFT) were used to calculate the electric band structure and density of states.[35,36] The generalized gradient approximation (GGA) of Perdew, Burke, and Ernzerhof (PBE) were employed to account for electron exchange and correlation.[37–39] For the model of alloy, the Zn atom was doped into 2×3 super cell of SnS_2 at Sn position with the Zn:Sn ratio of 1:5, which is consistent with the experimental conditions. All calculations were performed using a plane-wave cutoff energy of 450 eV. To prevent interactions between adjacent slabs, a vacuum spacing exceeding 20 Å was implemented along the vertical direction. Each structure was thoroughly relaxed until the forces converged to within 0.02 eV/Å. The electric structure and DOS of monolayer and bulk $Zn_{0.167}Sn_{0.833}S_2$ alloy are shown in Figs. 5(a) and 5(b) respectively. It is evident that both the monolayer and bulk alloy crystals exhibit a direct bandgap, with values of 1.458 eV and 1.507 eV, respectively. The bandgap of $Zn_{0.167}Sn_{0.833}S_2$ alloy is smaller than that of reported SnS_2, demonstrating that doping engineering is an effective strategy for modulating the band structure. The direct band gap of alloy arises from the presence of Zn atoms in the alloy belonging to Zn^{2+} state, which introduce defective states and adjust the top of valence band to Γ point. Additionally, the Zn atom's contribution significantly increases the density of states in the valence band.

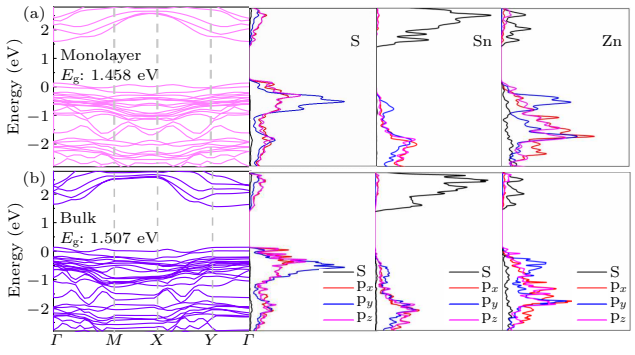


Fig. 5. The electric band structure of alloy. The calculated band structures and total density of states (TDOS) of monolayer $Zn_{0.167}Sn_{0.833}S_2$ (a) and bulk $Zn_{0.167}Sn_{0.833}S_2$ (b).

4. Conclusion

In summary, we have demonstrated the successful synthesis of the metal-site substitution alloy $Zn_{0.167}Sn_{0.833}S_2$ using the CVT method, achieving notable improvements in both photoresponsivity and electrical transport characteristics. Through a combination of EDS, Raman spectroscopy, XPS, and TEM, we verified the uniform incorporation of Zn atoms within the alloy matrix. The alloy based photodetector exhibit excellent linear dynamic range value of 80 dB, which is four times higher than SnS_2. The electron mobility of $Zn_{0.167}Sn_{0.833}S_2$ alloy is six times higher than SnS_2. These findings underscore the potential of $Zn_{0.167}Sn_{0.833}S_2$ alloys to drive advancements in optoelectronic and photodetection technologies, paving the way for high-performance semiconductor applications.

Acknowledgements

Project supported by the Beijing Natural Science Foundation (Grant No. Z220005), the National Key Research and Development Program of China (Grant Nos. 2022YFB3606902 and 2022YFA1405600), and the National Natural Science Foundation of China (Grant No. 12274456) by the Opening Project of the Laboratory of Microelectronic Devices & Integrated Technology, Chinese Academy of Sciences (CAS), Institute of Microelectronics, Chinese Academy of Sciences.

References

[1] Kim J, Pankow R M, Cho Y, *et al*. 2024 *Nat. Electron.* **7** 234
[2] Zhang K, She Y, Cai X, *et al*. 2023 *Nat. Nanotechnol.* **18** 48
[3] Zhou S, Bao C, Fan B, *et al*. 2023 *Nature* **614** 75
[4] Yang P, Wang D, Zhao X, *et al*. 2022 *Nat. Commun.* **13** 3238
[5] Zhou Z, Shen T, Wang P, *et al*. 2023 *Sci. Bull.* **68** 173
[6] Zhou Z, Cui Y, Tan P H, *et al*. 2019 *J. Semicond.* **40** 061001
[7] Wang B, Tang Z, Zheng H, *et al*. 2023 *Chin. Phys. B* **32** 098508
[8] Wang Z, Tan C, Peng M, *et al*. 2024 *Light Sci. Appl.* **13** 277
[9] Giri A, Park G and Jeong U 2023 *Chem. Rev.* **123** 3329
[10] Xin K, Li L, Zhou Z, *et al*. 2024 *Nat. Synth.* **3** 1176
[11] Gao H, Zhou H, Hao Y, *et al*. 2023 *J. Semicond.* **44** 122001
[12] Zhao T, Guo J, Li T, *et al*. 2023 *Chem. Soc. Rev.* **52** 1650
[13] Xue G, Qin B, Ma C, *et al*. 2024 *Chem. Rev.* **124** 9785
[14] Xie Y, Liang F, Chi S, *et al*. 2020 *ACS Appl. Mater. Interfaces* **12** 7351
[15] Wang B, Xing Y, Dong S, *et al*. 2023 *Chin. Phys. B* **32** 098504
[16] Wang H C, Lin Y, Liu X, *et al*. 2023 *Chin. Phys. B* **32** 018504
[17] Dong C, An X, Wu Z, *et al*. 2023 *J. Semicond.* **44** 112001
[18] Wang X, Pan L, Yang J, *et al*. 2021 *Adv. Mater.* **33** 2006908
[19] Zuo Y, Liu C, Ding L, *et al*. 2022 *Nat. Commun.* **13** 1007
[20] Mann J, Ma Q, Odenthal P M, *et al*. 2014 *Adv. Mater.* **26** 399
[21] Song J-G, Ryu G H, Lee S J, *et al*. 2015 *Nat. Commun.* **6** 7817
[22] Wang F, Gao T, Zhang Q, *et al*. 2018 *Adv. Mater.* **31** 1806306
[23] Huang Y, Sutter E, Sadowski J, *et al*. 2014 *ACS Nano* **8** 10743
[24] De D, Manongdo J, See S, *et al*. 2013 *Nanotechnology* **24** 025202
[25] Jia X, Tang C, Pan R, *et al*. 2018 *ACS Appl. Mater. Interfaces* **10** 18073
[26] Patil S G and H T R 1971 *J. Phys. D: Appl. Phys.* **4** 718
[27] Domingo G, Itoga R S and Kannewurf C R 1966 *Phys. Rev.* **143** 536
[28] Zhou Z, Long M, Pan L, *et al.* 2018 *ACS Nano* **12** 12416
[29] Zhang X, Tan Q H, Wu J B, *et al*. 2016 *Nanoscale* **8** 6435
[30] Ribeiro H B, Pimenta M A and Matos C J S 2018 *J. Raman. Spectrosc.* **49** 76
[31] Sriv T, Kim K and Cheong H 2018 *Sci. Rep.* **8** 10194
[32] Prasad N and Karthikeyan B 2019 *Nanoscale* **11** 4948
[33] Zhou X, Zhang Q, Gan L, *et al*. 2016 *Adv. Funct. Mater.* **26** 4405
[34] Gao L, Chen C, Zeng K, *et al.* 2016 *Light Sci. Appl.* **5** e16126
[35] Ricci F, Chen W, Aydemir U, *et al*. 2017 *Sci. Data.* **4** 170085
[36] Fuh H R, Chang C R, Wang Y K, *et al*. 2016 *Sci. Rep.* **6** 32625
[37] Yuan J, Xie Q, Yu N, *et al*. 2017 *Appl. Surf. Sci.* **394** 625
[38] Ryabov A, Akhatov I and Zhilyaev P 2020 *Sci. Rep.* **10** 8000
[39] Huang L, Zhong M, Deng H, *et al*. 2018 *Sci. China- Phys. Mech.* **62** 037311